Draft version January 6, 2016
Preprint typeset using LaTeX style emulateapj v. 5/2/11

AN INTERMEDIATE TYPE IA SUPERNOVA BETWEEN NORMAL AND SUPER-CHANDRASEKHAR

Yi Cao[1], J. Johansson[2], Peter E. Nugent[3,4], A. Goobar[5], Jakob Nordin[6], S. R. Kulkarni[1], S. Bradley Cenko[7,8], Ori Fox[9], Mansi M. Kasliwal[1,10], C. Fremling[11], R. Amanullah[5], E. Y. Hsiao[12,13], D. A. Perley[1], Brian D. Bue[14], Frank J. Masci[15], William H. Lee[16], Nicolas Chotard[17]

Draft version January 6, 2016

ABSTRACT

While recent observations provide evidence that super-Chandrasekhar Type Ia supernovae and at least a fraction of normal Type Ia supernovae probably originate from double-degenerate systems, these two subclasses show distinct characteristics observationally. Here we report an intermediate supernova iPTF13asv that may bridge this gap. On the one hand, similar to normal Type Ia supernovae, the over-luminous iPTF13asv follows the empirical relation between the peak magnitude, the lightcurve shape and its intrinsic color, and shows a near-IR secondary maximum like normal supernovae. On the other hand, similar to super-Chandrasekhar events, it has strong UV emission around maximum, low expansion velocities and persistent carbon absorption. We estimate a ^{56}Ni mass of $0.81^{+0.10}_{-0.18} M_{\odot}$ and a total ejecta mass of $1.44^{+0.44}_{-0.12} M_{\odot}$. Despite these similarities, iPTF13asv lacks iron absorption in its early-phase spectra, indicating a stratified ejecta structure with weak mixing. Based on the strong stratification of the ejecta and the similarity to super-Chandrasekhar events, we infer that iPTF13asv probably originates from a double-degenerate system.

Subject headings: supernovae: general – supernovae: individual (iPTF13asv) – ultraviolet: general

1. INTRODUCTION

Type Ia supernovae (SNe) are thermonuclear explosions of carbon oxygen white dwarfs (WDs). Since the majority of them (normal Type Ia SNe) follow a well-established empirical relation between variation of their peak magnitudes and lightcurve shapes (Phillips 1993), they are standardized to measure cosmological distances (see Goobar & Leibundgut 2011 for a review). However, the underlying progenitor systems and explosion mechanisms of Type Ia SNe remain poorly understood.

Recent observations have provided mounting evidence that Type Ia SNe have multiple progenitor channels (see Maoz et al. 2014 for a review). In the single-degenerate (SD) channel, a WD accretes material from a companion star and explodes when its mass approaches the Chandrasekhar limit (Whelan & Iben 1973). This channel is supported by possible detections of companion stars in pre- or post-SN images (McCully et al. 2014; Foley et al. 2014), likely signatures of supernova-companion collisions (Cao et al. 2015; Marion et al. 2015), and observations of variable Na I D absorption (Patat et al. 2007; Sternberg et al. 2014). In the double-degenerate (DD) channel, in contrast, two WDs collide or merge in a binary or even triple system to produce a Type Ia SN (e.g., Nomoto & Iben 1985; Kushnir et al. 2013). This channel is consistent with observations of two nearby Type Ia SN2011fe and SN2014J (e.g., Li et al. 2011; Brown et al. 2012; Shappee et al. 2013; Margutti et al. 2014; Kelly et al. 2014; Goobar et al. 2015; Lundqvist et al. 2015).

Unlike the SD channel, SNe from the DD channel may have ejecta mass beyond the Chandrasekhar limit (super-Chandrasekhar Type Ia SNe). In fact, more than a handful of SNe were found to have total ejecta masses significantly exceeding the Chandrasekhar limit (Howell et al. 2006; Hicken et al. 2007; Yuan et al. 2010; Yamanaka et al. 2009; Scalzo et al. 2010; Silverman et al. 2011; Scalzo et al. 2014c). However, these super-Chandrasekhar SNe show distinctive characteristics compared to normal events: they are over-luminous in both the optical and UV, implying a large amount of synthesized ^{56}Ni. They show low expansion velocities and long rise times, leading to massive ejecta. They also show persistent absorption from unburned carbon. If they origi-

[1] Astronomy Department, California Institute of Technology, Pasadena, CA 91125, USA
[2] Benoziyo Center for Astrophysics, Weizmann Institute of Science, 76100 Rehovot, Israel
[3] Computational Cosmology Center, Computational Research Division, Lawrence Berkeley National Laboratory, 1 Cyclotron Road, MS 50B-4206, Berkeley, CA 94720, USA
[4] Department of Astronomy, University of California Berkeley, Berkeley, CA 94720-3411, USA
[5] Oskar Klein Centre, Physics Department, Stockholm University, SE-106 91 Stockholm, Sweden
[6] Institut für Physik, Humboldt-Universität zu Berlin, Newtonstr. 15, 12489 Berlin, Germany
[7] Astrophysics Science Division, NASA Goddard Space Flight Center, Mail Code 661, Greenbelt, Maryland 20771, USA
[8] Joint Space-Science Institute, University of Maryland, College Park, MD 20742, USA
[9] Space Telescope Science Institute, 3700 San Martin Drive, Baltimore, MD 21218, USA
[10] Observatories of the Carnegie Institution for Science, 813 Santa Barbara Street, Pasadena, California 91101, USA
[11] Department of Astronomy, The Oskar Klein Center, Stockholm University, AlbaNova, 10691 Stockholm, Sweden
[12] Department of Physics, Florida State University, Tallahassee, FL 32306, USA
[13] Department of Physics and Astronomy, Aarhus University, Ny Munkegade 120, 8000 Aarhus C, Denmark
[14] Jet Propulsion Laboratory, California Institute of Technology, Pasadena, CA 91125, USA
[15] Infrared Processing and Analysis Center, California Institute of Technology, MS 100-22, Pasadena, CA 91125, USA
[16] Instituto de Astronomía, Universidad Nacional Autónoma de México, Apdo. Postal 70-264 Cd. Universitaria, México DF 04510, México
[17] Université de Lyon, F-69622, France ; Université de Lyon 1, Villeurbanne ; CNRS/IN2P3, Institut de Physique Nucléaire de Lyon

nate from the same DD systems as some normal Type Ia SNe, then an intermediate case is needed to bridge the super-Chandrasekhar and normal Type Ia SNe.

In this paper, we present observations of a peculiar Type Ia SN, iPTF13asv, that shares observational characteristics with both super-Chandrasekhar and normal Type Ia SN. It was discovered with $r = 20.54 \pm 0.16$ mag at $\alpha = 16^h22^m43^s.19$, $\delta = +18°57'35''.0$ (J2000) in the vicinity of galaxy SDSS J162243.02+185733.8 on UTC 2013 May 1.44 (hereafter May 1.44) by the intermediate Palomar Transient Factory (iPTF; Law et al. 2009; Rau et al. 2009). Nothing was seen at the same location down to 5-σ detection thresholds of $r \simeq 21.0$ mag on images taken on April 30.5 and earlier. iPTF13asv was independently discovered and classified as a peculiar Type Ia by Zhou et al. (2013), and was designated as SN2013cv.

This paper is organized as follows: the observational data is present in §2. The photometric and spectroscopic properties are analyzed in §3, and we construct its bolometric lightcurve and estimate the total ejecta mass in §4. A discussions about the nature of iPTF13asv is given in §5 and our conclusions are summarized in §6.

Throughout this paper, we adopt a Hubble Constant $H_0 = 67.77\,\mathrm{km\,s^{-1}\,Mpc^{-1}}$ (Planck Collaboration et al. 2013). The apparent host galaxy of iPTF13asv does not have a redshift-independent distance measurement in the NASA/IPAC Extragalactic Database. Thus we calculate a distance modulus of 36.07 mag by using its redshift 0.036. The peculiar motion of the host galaxy at $\sim$100 km s^{-1} introduces an uncertainty of $\lesssim 0.05$ mag to the distance modulus. The Galactic line-of-sight extinction is $E(B-V) = 0.045$ (Schlafly & Finkbeiner 2011). We correct for the Galactic extinction by using the parametrized model in Fitzpatrick (1999) with $R_V = 3.1$.

2. OBSERVATIONS

The nightly-cadence survey of iPTF (weather-permitting) with the 48-inch telescope at Palomar Observatories (P48) provides a well-sampled R-band light curve of iPTF13asv covering the pre-SN history and its rise phase. After discovery, we also utilized the Palomar 60-inch telescope (P60; Cenko et al. 2006), Andalusia Faint Object Spectrograph and Camera (ALFOSC) on the Nordic Optical Telescope (NOT), and the RATIR camera mounted on the OAN/SPM 1.5-meter Harold L. Johnson telescope for multi-band photometric follow-up observations. We also triggered target-of-opportunity observations of the *Swift* spacecraft for X-ray and UV follow-up. A sample of the ground-based photometric measurements are presented in Table 1 and the space-based measurements in Table 2.

Spectroscopic observations were undertaken with the SuperNova Integral Field Spectragraph (SNIFS; Lantz et al. 2004) on the 2.2 m telescope of the University of Hawaii, the Dual Imaging Spectrograph (DIS) on the ARC 3.5 m telescope at Apache Point Observatory (APO), the Double Spectrograph (DBSP; Oke & Gunn 1982) on the 200-inch Hale telescope (P200) at Palomar Observatory, and the Folded-port InfraRed Echellette (FIRE) on the Magellan-I Baade Telescope at Las Campanas Observatory. As presented in Figure 2, the spectral sequence provides temporal coverage of the SN evolution.

Table 1
Plhotometry of iPTF13asv

Tel./Inst.[1]	filter	MJD−56000 (day)	mag.[2]	mag. err.
P48	PTF-R	412.456	>20.35	...
P48	PTF-R	413.442	20.44	0.17
P48	PTF-R	413.471	20.34	0.16
P48	PTF-R	414.470	19.58	0.09
P48	PTF-R	415.469	19.06	0.06
		...		

[1] This column lists the telescopes and instruments used for photometric observations of iPTF13asv. We built reference images by stacking pre-SN or post-SN frames and used image subtraction technique to remove light contamination from the host galaxy. Point-spread-function (PSF) photometry is performed on subtracted images. The photometry is calibrated either to SDSS or by observing Landolt photometric standard stars.
[2] Conventionally, the magnitudes in $UBVJH$ bands are in Vega system. Those in other bands are in AB system. No extinction is corrected in this column.

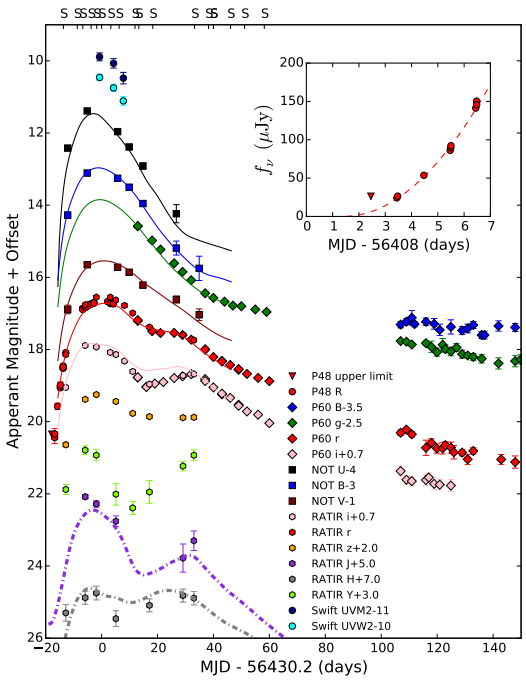

Figure 1. Multi-color light curve of iPTF13asv. Colors and shapes represent different filters and instruments, respectively. A deviation of $\simeq 0.1$ mag between P48 R-band (red circles) and P60 r-band (red diamonds) is due to the difference between the P48 Mould R filter and the P60 SDSS r filter. The "S" ticks on the top axis denote spectroscopic observation epochs. The solid curves are SALT2 best-fit lightcurves in corresponding filters. The dash-dotted curves are the IR template from Stanishev et al. (2015). The inset zooms into the very early phases of the PTF R-band lightcurve. The dashed curve in the inset shows the best t^2 law fit to the early lightcurve.

The lightcurve and spectra are made publicly available via WISeREP[18] (Yaron & Gal-Yam 2012).

[18] WISeREP is available at http://www.weizmann.ac.il/

Table 2
Swift Observations

Obs. Date	UVOT (AB mag)[1] *uvm2*	*uvw2*	XRT (cnt/s)[2]
May 17.4	21.02 ± 0.08	20.59 ± 0.08	$< 3.6 \times 10^{-3}$
May 22.6	21.25 ± 0.10	20.92 ± 0.09	$< 8.0 \times 10^{-3}$
May 25.9	21.83 ± 0.12	21.39 ± 0.10	$< 4.3 \times 10^{-3}$
June 02.7	< 22.20	< 22.36	$< 9.0 \times 10^{-3}$
June 10.5	< 21.98	< 22.18	$< 1.2 \times 10^{-2}$
June 13.4	< 22.37	< 22.46	$< 8.7 \times 10^{-3}$

[1] We used the `HEASoft` package to perform aperture photometry on the UVOT images. The photometry is corrected for coincident loss and with the PSF growth curve, and calibrated with the latest calibration (Breeveld et al. 2011). In order to remove host galaxy contamination in the photometric measurements, we acquired post-SN reference frames. In cases of non-detection, we estimated 5-σ upper limits.
[2] We used the `XImage` software to analyze the XRT data. In cases of non-detection, we estimate upper limits with a 99.7% confidence level.

3. ANALYSIS

3.1. *Initial Rise and Explosion Date*

In order to determine the explosion date of iPTF13asv, we follow Nugent et al. (2011) and model the early PTF-R-band lightcurve of iPTF13asv as a freely expanding fireball where the luminosity increases as $\propto t^2$ and the temperature remains constant. Restricting ourselves to the lightcurve within four days of discovery, we find a best fit (the inset in Figure 1) at an explosion date of April 29.4 ± 0.3 (95% confidence interval) with a fitting $\chi^2 = 4.3$ for five degrees of freedom. The best-fit light curve is also consistent with the upper limit on April 30.4.

If we replace the t^2 model with a power-law model, we obtain strong degeneracy between the explosion date and the power-law index over a large range of the parameter space. For simplicity, we use the explosion date determined in the t^2 model in the following analysis.

A caveat here is that there might be a dark time between the SN explosion and the time when it becomes visible (Piro 2012; Piro & Morozova 2015). The length of the dark time is roughly the diffusive timescale for the shallowest ^{56}Ni layer in the ejecta.

3.2. *Lightcurve*

In order to determine the lightcurve shape parameters of iPTF13asv, we use the SALT2 software (Guy et al. 2007) to fit its optical lightcurve. The best-fit lightcurve gives a rest-frame B-band peak magnitude $m_B = 16.28 \pm 0.03$ on May 18.12 ± 0.09. We set this B-band peak date as $t = 0$ in the rest of this paper. The fit also gives a color term $c = -0.16 \pm 0.02$, and two shape parameters $x_0 = 0.0055 \pm 0.0001$ and $x_1 = 0.37 \pm 0.09$. Based on the fitted SALT2 light curve, we derive a color $(B-V)_0 = -0.14 \pm 0.03$ at the B-band maximum. We also obtain $\Delta m_{15} = 1.03 \pm 0.01$ from x_1 by using the relation in Guy et al. (2007).

The local extinction in the host galaxy of iPTF13asv is probably small for several reasons. First, as shown in Figure 3, iPTF13asv and SN2011fe have a similar B−V color around maximum. The difference of the B−V colors between 0 and +30 days is probably correlated with the different stretch of these two events (Nobili & Goobar 2008). Since SN2011fe is unreddened by its host (Nugent et al. 2011; Vinkó et al. 2012), iPTF13asv also has little local extinction. Second, the intrinsic color $B - V = 0.95$ mag of iPTF13asv at +35 days are consistent with the latest calibration of the Lira relation (Burns

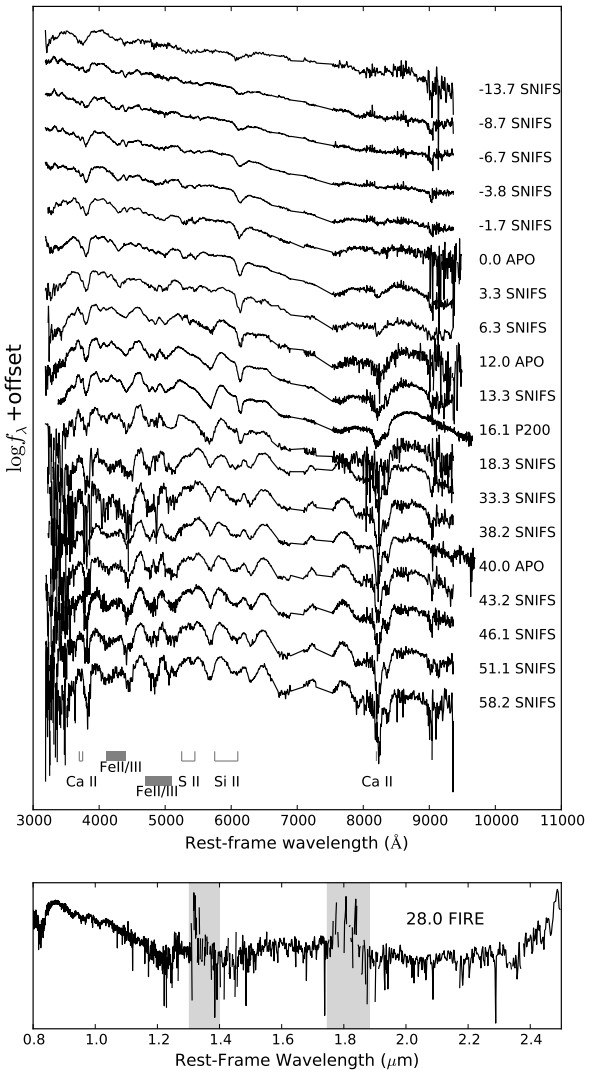

Figure 2. Optical and near-IR spectral evolution of iPTF13asv. Ticks at the bottom denote the main spectral features. The phases and telescopes/instruments are labeled to the right of corresponding spectra. The long-slit spectra taken by APO/DIS, P200/DBSP and Magellan/FIRE are extracted through usual procedures in IRAF and/or IDL and calibrated using observations of spectroscopic stars. Data reduction of SNIFS is outlined in Aldering et al. (2006). However, due to bad weather, flux calibration of SNIFS spectra was not complete. Therefore, we interpolate the multi-band lightcurve and "warp" the spectra with low-order polynomials to match photometric data.

`astrophysics/wiserep/`.

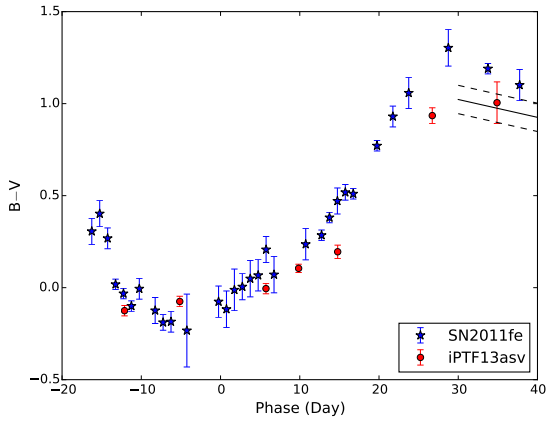

Figure 3. B−V color evolution of SN2011fe and iPTF13asv after correction for Galactic extinction The solid line shows the Lira relation from Burns et al. (2014) and the dashed lines corresponding to its 0.06 mag scattering.

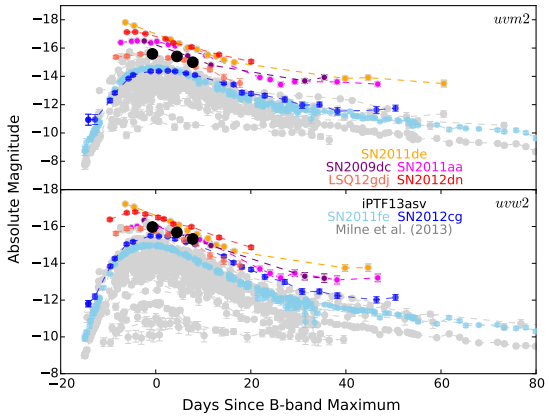

Figure 4. UV lightcurve comparison between iPTF13asv and other SNe Ia. A sample of SNe Ia from Milne et al. (2013) are shown in gray. Highlighted by different colors are lightcurves of iPTF13asv (black), SN2011fe (sky blue), SN2012cg (blue), super-Chandrasekhar events SN2009dc, SN2011aa and LSQ12gdj (purple), and the most UV-luminous event SN2011de (orange). All magnitudes are in the AB system.

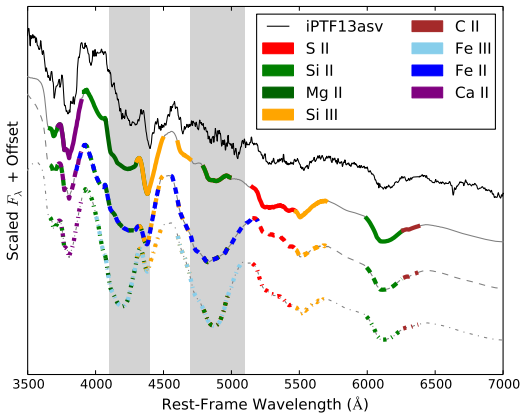

Figure 5. SYN++ synthetic SN spectrum fit to iPTF13asv at -9.2 days. From top to bottom are the observed spectrum, the synthetic spectrum without Fe (solid), the synthetic spectrum with Fe II (dashed) and the synthetic spectrum with Fe III (dash-dotted). The absorption features from different species are illustrated in different colors. The Fe II and Fe III absorption wavelength ranges are highlighted in light gray.

et al. 2014). Third, the absence of Na ID absorption in the low-resolution optical spectra also implies weak extinction in the host galaxy (Poznanski et al. 2012). Therefore, in what follows we neglect the local extinction correction.

After correction for Galactic extinction and including the distance uncertainty, we derive an absolute peak magnitude of iPTF13asv in its rest-frame B-band to be -19.97 ± 0.06. This is about 0.7 mag brighter than normal Type Ia SNe.

In the UV, iPTF13asv is very luminous around peak. As shown in Figure 4, iPTF13asv has UV lightcurves of both $uvm2$ and $uvw2$ filters similar to many super-Chandrasekhar events, and brighter than all other events except for SN2009dc (Brown 2014). In this comparison, no K-correction was made to iPTF13asv and the other SNe because K-correction is very small for low-redshift SNe. We note that calculations using the Nugent SN Ia template (Nugent et al. 2002) and the *HST* spectra of SN2011fe (Mazzali et al. 2014) show that at this redshift the K-correction is < 0.2 mag in both filters and thus these comparisons are good to $\lesssim 20\%$. It is also worth noting that SN2011fe belongs to the NUV-blue subclass (Brown et al. 2012; Milne et al. 2013). Since iPTF13asv and SN2011fe have similar an optical color and iPTF13asv is brighter in the UV than SN2011fe, iPTF13asv also has a very blue UV-optical color, similar to other super-Chandrasekhar events (Brown et al. 2014).

We also compare the IR lightcurves of iPTF13asv in the J- and H-band to the most recent lightcurve template for normal Type Ia events (Figure 1; Stanishev et al. 2015) and find that the sparsely-sampled lightcurves of iPTF13asv roughly follow the template. The peak magnitudes of iPTF13asv is $M_J = -18.97 \pm 0.08$ and $M_H = -18.30 \pm 0.19$, compared to the median peak magnitudes of $M_J = -18.39$ and $M_H = -18.36$ with rms scatters of $\sigma_J = 0.116 \pm 0.027$ and $\sigma_H = 0.085 \pm 0.16$ for normal Type Ia SNe (Barone-Nugent et al. 2012). Without a IR spectrum around maximum, it is difficult to interpret why iPTF13asv is so bright in the J band. Both J-band and H-band lightcurves show clear secondary maxima, indicating concentration of iron group elements in the central region of the iPTF13asv ejecta (Kasen 2006).

3.3. *Spectra*

As a result of nucleosynthesis and mixing during SN explosions, iron absorption is commonly seen in SN spectra, either as Fe II at low effective temperatures or as Fe III at higher temperatures. However, neither of these iron features are present in the early-phase spectra of iPTF13asv. As highlighted in gray regions of Figure 5, spectral feature identification with SYN++ (Thomas et al. 2011a) on the iPTF13asv spectrum at −8.7 days shows no Fe II or Fe III. We also compare the iPTF13asv spectra against both normal events (Figure 6 and super-Chandrasekhar events (Figure 7) to illustrate that, unlike iPTF13asv, both normal and super-Chandrasekhar SNe have iron absorption features at very early phases.

The absence of iron at early phases indicates that syn-

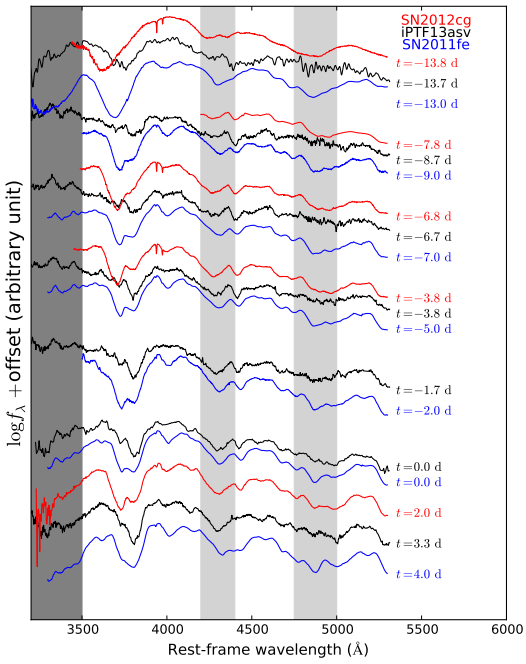

Figure 6. Blue spectral comparison of iPTF13asv to SN2011fe and SN2012cg. The spectra of iPTF13asv between 3200 Å and 5300 Å (black) are compared with those of normal SN2011fe (blue) and over-luminous SN2012cg (red) at similar phases. The gray color highlights the UV region and the light gray color indicates the ion absorption features.

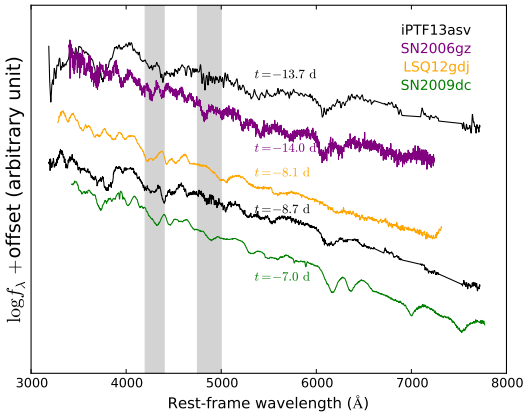

Figure 7. Comparison of earliest spectra between iPTF13asv and super-Chandrasekhar events. The earliest two spectra of iPTF13asv (black) are compared to SN2006gz at −14 days (purple), SN2009dc at −7 days (green), and LSQ12gdj at −8 days (orange). The wavelength ranges for absorptions of Fe II and Fe III are highlighted in light gray.

thesized iron group elements are confined in low-velocity regions of the ejecta. Since the iron group elements are the main absorbers of photons below 3500 Å, the lack of iron group elements in fast-moving ejecta effectively reduces the UV opacity at early phases. In fact, as shown in the dark gray region in Figure 6, the flux of iPTF13asv below 3500 Å is seemingly stronger than those

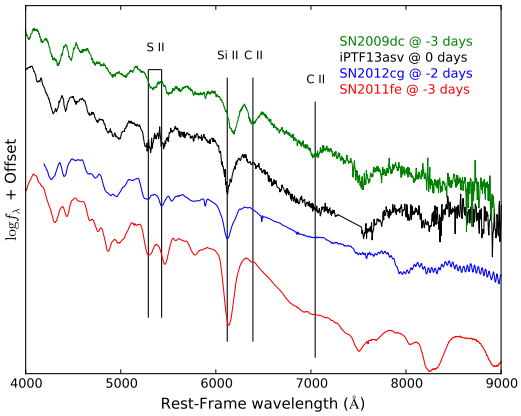

Figure 8. Spectral cross-matching. The spectrum of iPTF13asv around maximum matches those of SN2011fe, SN2012cg and SN2009dc (super-Chandrasekhar).

of SN2011fe at early phases. We did not trigger *Swift* observations at early phases of iPTF13asv, because it is about 160 Mpc away from us. Our experience shows that *Swift* UV observations are usually sensitive to Type Ia SNe within 100 Mpc. Otherwise, *Swift* observations at these phases would be perfectly suited to show the UV flux difference.

The spectral sequence in Figure 6 also shows that the iron features start to emerge in iPTF13asv about a week before maximum. Around maximum, the spectra of iPTF13asv show similar features to both normal and super-Chandrasekhar events (Figure 8). The expansion velocities of iPTF13asv, as indicated by Si II 6355 minima, are similar to those of both SN2011fe and SN2012cg and higher than that of SN2009dc.

We further compare the expansion velocity evolution of iPTF13asv to a sample of normal and super-Chandrasekhar events (Figure 9). The velocities are measured by fitting a Gaussian profile to the iPTF13asv spectra around the Si II 6355 features. The continuum components are removed by a linear regression to regions at both sides of the absorption features. As can be seen in Figure 9, iPTF13asv has a low expansion velocity and a shallow velocity gradient, compared to normal Type Ia SNe. Around maximum, the expansion velocity of iPTF13asv is $\simeq 10,000\,\mathrm{km\,s^{-1}}$ and the velocity gradient is roughly zero. The low expansion velocity and shallow velocity gradient of iPTF13asv is usually seen in super-Chandrasekhar events.

We also note that iPTF13asv shows weak but persistent C II absorption features between −14.1 and +11.5 days (Figure 10). The velocities of these C II lines change from $\simeq 14,000\,\mathrm{km\,s^{-1}}$ at −14.1 days to $\simeq 9,000\,\mathrm{km\,s^{-1}}$. In comparison, about 30% of normal SNe show the C II 6580 and C II 7234 absorption notches in early phases (Thomas et al. 2011b; Parrent et al. 2011; Silverman & Filippenko 2012), but these C II features usually disappear before maximum. In contrast, super-Chandrasekhar events usually show strong and persistent C II features after maximum.

3.4. *Host Galaxy*

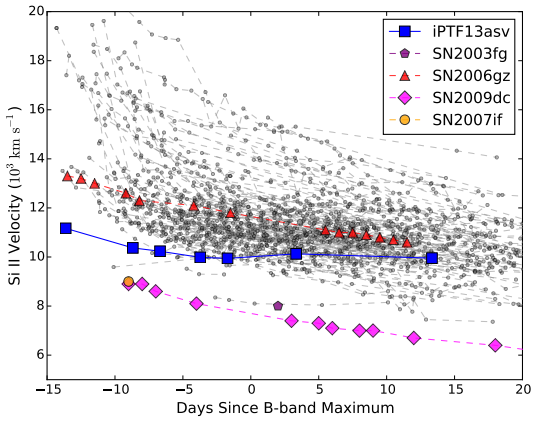

Figure 9. Si II velocity evolution of iPTF13asv and other SNe Ia. The gray points are from a large sample of mostly normal SNe Ia in Foley et al. (2011). Blue squares represent iPTF13asv and other color symbols as shown in the legend represent super-Chandrasekhar events.

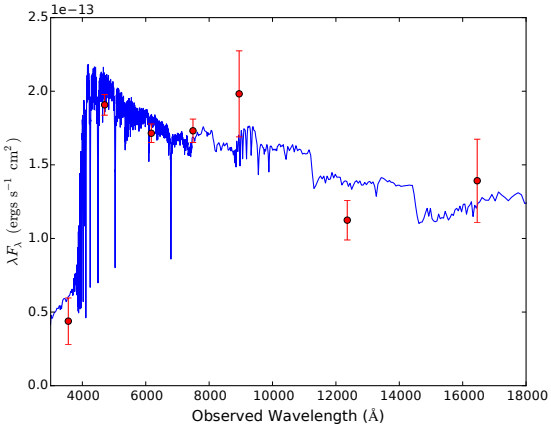

Figure 11. SED fit of the host galaxy. The data points (red) are SDSS model magnitudes in optical and aperture-photometric measurements in the near-IR RATIR reference images. The blue spectrum is the best fit from FAST.

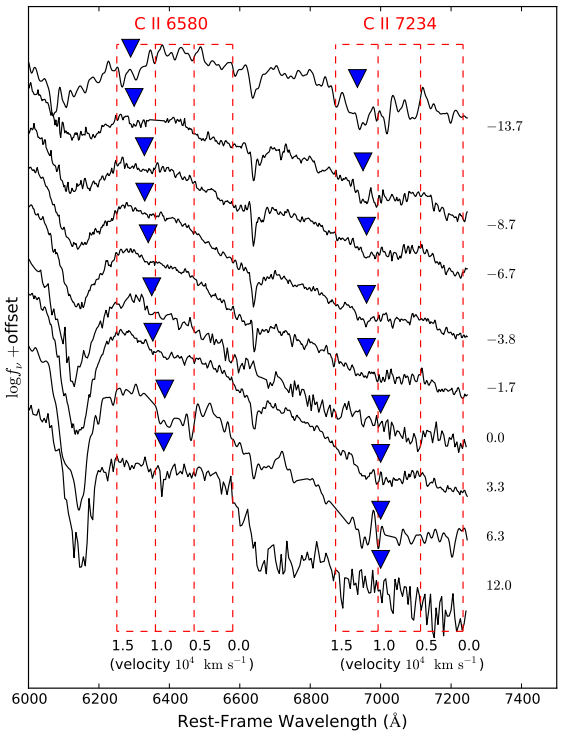

Figure 10. Carbon features of iPTF13asv at different phases. The numbers to the right of each spectrum indicate the phases in days. The blue triangles point to the carbon features. The red dashed axes show velocities of C II 6580 and C II 7234 lines.

After iPTF13asv faded away, we obtained a low signal-to-noise ratio spectrum of its apparent host galaxy SDSS J162254.02+185733.8. The spectrum only shows Hα emission at the redshift of iPTF13asv. We fit a Gaussian profile to the Hα line and measure a luminosity of 3×10^{38} ergs s^{-1}. We adopt the empirical relation between Hα luminosity and star formation rate (Kennicutt 1998) and obtain a star formation rate of $2 \times 10^{-3}\,M_\odot\,\mathrm{yr}^{-1}$ for the host galaxy.

Next, we construct the spectral energy distribution (SED) of the host galaxy with optical photometry from SDSS and near-IR photometry measured on the SN reference images. The SED is then modeled with a galaxy synthesis code called the Fitting and Assessment of Synthetic Templates (FAST; Kriek et al. 2009) assuming an exponentially decaying star formation history and a solar metallicity. The best fit model gives a galaxy age of $10^{8.6}$ years and a stellar mass of $10^{7.8} M_\odot$ with a reduced $\chi^2 = 1.6$ (Figure 11). The best fit model also shows no ongoing star forming activity. Because SED fitting models are usually insensitive to very low star forming rates, the best fit model is consistent with the low star formation rate derived from the Hα flux.

The derived star formation rate and the stellar mass of the iPTF13asv host galaxy follow the empirical relation between stellar mass and star formation rate (Foster et al. 2012). Using the mass-metallicity relation (Foster et al. 2012), we also estimate a gas-phase metallicity of $12 + \log(\mathrm{O/H}) \sim 8$ for the host galaxy. Compared to the host galaxy sample of SNe Ia in Pan et al. (2014), SDSS J162254.02+185733.8 is one of the least massive and most metal-poor galaxies that host Type Ia SNe.

4. BOLOMETRIC LIGHTCURVE AND EJECTA MASS

4.1. *Bolometric Lightcurve*

Given the wavelength coverage of the iPTF13asv spectra, we first construct a pseudo-bolometric lightcurve between 3500 Å and 9700 Å. In order to calibrate the absolute fluxes of these spectra, we use interpolated optical lightcurves to "warp" the spectra. Then the spectra are integrated to derive the pesudo-bolometric lightcurve.

Due to the sparsely sampled UV and IR lightcurves, it is difficult to estimate the UV and IR radiation at different phases. Therefore we calculate optical-to-bolometric correction factors with a spectral template (Hsiao et al. 2007). In this calculation, we find that the UV correction reaches about 25% before the B-band maximum and

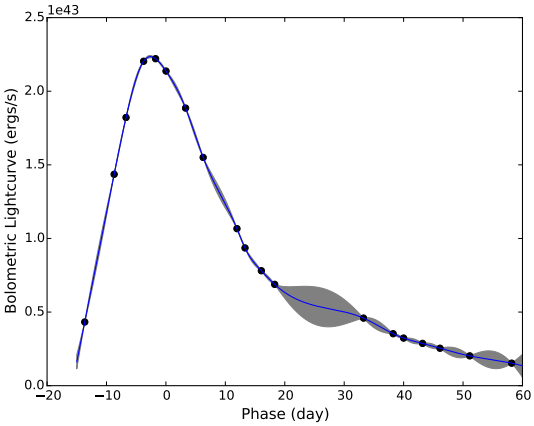

Figure 12. Bolometric lightcurve. The measured bolometric luminosities at different phases are in black circles. The blue curve is the best fit from the Gaussian process regression. The gray region represents the 1-σ uncertainty of the regression curve.

quickly drops to less than 5% around and after the B-band maximum. Given the inference that the SN might be UV-luminous before maximum and the observational fact that the SN is among the UV-bright Type Ia SNe around maximum, our calculated correction probably underestimates the UV radiation. Using the Swift data around maximum, we estimate that this UV correction introduces a systematic uncertainty of a few percent to the bolometric luminosity. Around maximum when the SN cools down, the UV contribution to the bolometric luminosity becomes even less important.

In the IR, the correction above 9700 Å is below 10% around the B-band maximum, and then reaches a maximum of 24% around the secondary maximum in the near-IR. At the epochs with IR data, we find that the calculated correction is consistent with the IR measurements.

The final bolometric lightcurve is shown in Figure 12. We further employ Gaussian process regression to derive a maximum bolometric luminosity $L_{max} = (2.2 \pm 0.2) \times 10^{43}\,\mathrm{erg\,s^{-1}}$ at -2.6 days.

4.2. *^{56}Ni Mass and Ejecta Mass*

Next, we follow the procedure in Scalzo et al. (2012, 2014a) to derive the ^{56}Ni mass and the total ejecta mass. First, the ^{56}Ni mass can be estimated through the following equation

$$L_{max} = \alpha S(t_R)\ , \tag{1}$$

where $S(t_R)$ is the instantaneous radioactive power at the bolometric luminosity maximum. α is an efficiency factor of order unity, depending on the distribution of ^{56}Ni (Jeffery et al. 2006). We adopt a fiducial value of $\alpha = 1.3$ following Scalzo et al. (2012). The radioactive power of ^{56}Ni $\rightarrow^{56}$ Co $\rightarrow^{56}$ Fe is (Nadyozhin 1994)

$$S(t_r) = \left[6.31\exp\left(-t_r/8.8\right) + 1.43\exp\left(-t_r/111\right)\right] M_{\mathrm{Ni}}\ , \tag{2}$$

where $S(t)$ is in the unit of $10^{43}\,\mathrm{erg\,s^{-1}}$ and M_{Ni} is in the unit of $M_\odot$. With the measured maximum bolometric luminosity $L_{max} = (2.2 \pm 0.2) \times 10^{43}\,\mathrm{erg\,s^{-1}}$ at -2.6 days, we estimate a ^{56}Ni mass of $(0.77 \pm 0.07) M_\odot$.

About one month after the SN maximum, the SN debris expands approximately in a homologous manner. At this time, most ^{56}Ni atoms have decayed to ^{56}Co. Hence the total luminosity can be approximated by

$$L(t) = \left[1 - \exp(-(t_0/t)^2)\right] S_\gamma(t) + S_{e^+}(t)\ , \tag{3}$$

where S_γ and S_{e^+} are the decay energy of ^{56}Co carried by γ-ray photons and positions. At time t_0, the mean optical path of γ-ray photons becomes unity. For a given density and velocity profile, t_0 reflects the column density along the line of sight. We fit equation (3) to the bolometric lightcurve of iPTF13asv after +20 days and obtained $t_0 = 44.2 \pm 2.0$ days.

Next, we estimate the total ejecta mass of iPTF13asv. If we assume a density profile $\rho(v) \propto \exp(-v/v_e)$ where v_e is a scale velocity, then the ejecta mass can be expressed as

$$M_{ej} = \frac{8\pi}{\kappa_\gamma q} \left(v_e t_0\right)^2\ , \tag{4}$$

where κ_γ is the Compton scattering opacity for γ-ray photons . The value of κ_γ is expected to lie in the range between $0.025\,\mathrm{cm^2 g^{-1}}$ and $0.033\,\mathrm{cm^2 g^{-1}}$ (Swartz et al. 1995). We adopt a value of $0.025\,\mathrm{cm^2 g^{-1}}$ for the optically thin regime. The form factor q describes the distribution of ^{56}Ni and thus ^{56}Co (Jeffery 1999). For evenly mixed ^{56}Ni, the value of q is close to one third. Taking element stratification and mixing in the interfaces into account, Scalzo et al. (2014a) found that $q = 0.45 \pm 0.05$. Here, we adopt $q = 0.45$ in our estimation.

The value of v_e can be obtained by conservation of energy. The total kinetic energy of the ejecta is $6 M_{ej} v_e^2$. Neglecting the radiation energy, the total kinetic energy is equal to the difference between the nuclear energy released in the explosion and the binding energy of the exploding white dwarf. The binding energy of a rotating white dwarf with mass M_{ej} and central density ρ_c is given in Yoon & Langer (2005). Here we restrict the central density to lie between 10^7 and $10^{10}\,\mathrm{g\,cm^{-3}}$.

If we further assume that the ejecta is composed of unburned CO and synthesized Si, Fe and Ni, then the nuclear energy of the SN explosion is formulated in Maeda & Iwamoto (2009) as a function of mass M_{ej} and mass fractions f_{Fe}, f_{Ni} and f_{Si}. The ratio $\eta = f_{\mathrm{Ni}}/(f_{\mathrm{Ni}} + f_{\mathrm{Fe}})$ is also a function of ρ_c. Following Scalzo et al. (2014a), we adopt a Gaussian prior

$$\eta = 0.95 - 0.05\rho_{c,9} \pm 0.03\max(1, \rho_{c,9})\ , \tag{5}$$

where $\rho_{c,9}$ is ρ_c in units of $10^9\,\mathrm{g\,cm^{-3}}$. In addition, we restrict the mass fraction f_{CO} less than 10%.

Based on the above assumptions, with a given set of ejecta mass M_{ej}, central density ρ_c and the mass fractions of different elements, we can calculate the maximum bolometric luminosity and t_0 in equation (3) and compare them with our measurements of iPTF13asv. After one million Markov-Chain-Monte-Carlo iterations, we obtain $M_{Ni} = 0.81^{+0.10}_{-0.18}$ and $M_{ej} = 1.44^{+0.44}_{-0.12} M_\odot$ at a 95% confidence level.

4.3. *Detached Shell Surrounding the SN*

In order to explain the almost constant Si II velocity in super-Chandrasekhar events, Scalzo et al. (2010) and Scalzo et al. (2012) hypothesize a stationary shell detached from the ejecta. The shell is accelerated to a constant speed v_{sh} by colliding with fast-moving ejecta with

velocities greater than v_{sh}. In fact, some simulations of WD mergers show that the outermost material forms such a stationary envelope that collides with fast-moving ejecta (Hoeflich & Khokhlov 1996). Following the calculation procedure in Scalzo et al. (2010) and Scalzo et al. (2012), we derive an envelope mass of $0.15^{+0.11}_{-0.01} M_\odot$ for iPTF13asv.

Though the detached shell has little effect on the γ-ray opacity and peak luminosity of a SN, it reddens the SN and extends its rise time. However, compared to other super-Chandrasekhar events (Scalzo et al. 2012), iPTF13asv shows a blue intrinsic color and a much shorter rise time. Based on the color and rise time, we infer that iPTF13asv is unlikely to have this detached shell.

5. DISCUSSIONS

5.1. *Comparison To Super-Chandrasekhar And Normal Events*

In Table 3, we compare iPTF13asv against both super-Chandrasekhar and normal Type Ia SNe. In addition to the features listed in the table, the H-band break, which is formed by absorption of Fe II, Co II and Ni II (Hsiao et al. 2013), is distinctive between super-Chandrasekhar and normal events. The break usually appears in normal SNe within a month of maximum, but is absent in the super-Chandrasekhar events. However, in the case of iPTF13asv, the only near-IR spectrum is taken one month after the maximum, and is therefore not constraining to the existence of the H-band break.

As can be seen from the table, on the one hand, the over-luminous iPTF13asv has a normal lightcurve shape and near-IR secondary peak. On the other hand, like super-Chandrasekhar events, iPTF13asv shows persistent C II absorption and low expansion velocity with little evolution. While the derived ^{56}Ni mass is higher in iPTF13asv than in normal events, the total ejecta mass is close to the Chandrasekhar limit.

We further examine whether iPTF13asv follows the empirical relation between the peak magnitude, the lightcurve shape and the intrinsic color, i.e.,

$$\mu = m_B^* - (M_B - \alpha x_1 + \beta c) \ , \qquad (6)$$

where μ is the distance modulus, m_B^* is the observed peak magnitude in the rest-frame B band, α, β and M_B are free parameters. In order account for the dependence on the host galaxy properties, Sullivan et al. (2011) suggest to use different values of M_B for galaxies of stellar mass greater and less than $10^{10} M_\odot$. In the case of iPTF13asv, the stellar mass of its host galaxy is $\sim 10^{7.8} M_\odot$. For galaxies with stellar mass less than $10^{10} M_\odot$, Betoule et al. (2014) obtained $M_B = -19.04 \pm 0.01$, $\alpha = 0.141 \pm 0.006$ and $\beta = 3.101 \pm 0.075$. Substituting $m_B^* = 16.28 \pm 0.03$, $x_1 = 0.37 \pm 0.09$ and $c = -0.16 \pm 0.02$ into the empirical relation, we find that iPTF13asv still follows the empirical relation, whereas in contrast, super-Chandrasekhar events are outliers of this empirical relation (Scalzo et al. 2012).

Based on this comparison, we suggest that iPTF13asv is an intermediate Ia SN between normal and super-Chandrasekhar events, and it may represent the transition of observational properties as the total ejecta mass increases from Chandrasekhar to super-Chandrasekhar in the DD channel.

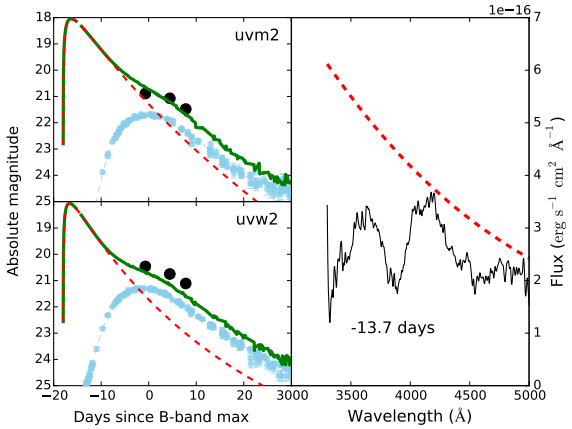

Figure 13. Comparison between the SN-companion interaction signature model and iPTF13asv data. *Left*: The *uvm*2 and *uvw*2 lightcurves of iPTF13asv (black circles) are compared to the total lightcurves (green) which combine the SN-companion interaction component (red; Kasen 2010) and the SN intrinsic emission (cyan). *Right*: the iPTF13asv spectrum at −13.7 days (black) is compared to the thermal spectrum of SN-companion collision (red).

In addition, Brown (2014) reported the UV brightest SN2011de. However, SN2011de is dissimilar to iPTF13asv, as it has a high-velocity component in its Si II line. The lack of a well-sampled lightcurve and a spectral sequence also makes it difficult to estimate the ^{56}Ni mass and total ejecta mass of SN2011de.

5.2. *Strong UV Emission*

Strong UV emission in a Type Ia SN can be powered by an extrinsic SN-companion collision (Kasen 2010) or intrinsic ^{56}Ni decay. In fact, in the UV-luminous SN2011de, Brown (2014) offered a possible explanation to its *Swift* lightcurve as a SN-companion collision. Hence, despite similarities between iPTF13asv and super-Chandrasekhar events, we assess whether the strong UV emission of iPTF13asv can be explained by collision between the SN and a companion star.

We utilize the scaling relation in Kasen (2010) to fit the observed *uvm*2 lightcurve. In order to account for the non-negligible emission from the SN itself, we use the well-sampled *uvm*2 lightcurve of SN2011fe as a template. The fitting result shows that the companion star is located at 2×10^{13} cm away from the exploding WD (left panel of Figure 13). Given a typical mass ratio of a few, the companion has a radius of $\sim 100 R_\odot$ to fill its Roche lobe.

Although the model fit to the UV lightcurve looks plausible, it overshoots the optical spectrum of iPTF13asv at −13.7 days at short wavelengths (right panel of Figure 13). The model also produces a pulse of $\simeq 200 \mu$Jy in the R-band within a few days of explosion, much stronger than the observed R-band fluxes $\lessapprox 150 \mu$Jy at the very early phases (the inset of Figure 1). Additionally, we caution that, as pointed out in Kasen (2010), this scaling relation may become invalid after the first few days of the SN explosion. Hence, we conclude that the strong UV emission seen in iPTF13asv is not produced by SN-companion collision.

Table 3
Comparison of iPTF13asv to normal and super-Chandrasekhar SNe

Feature	Normal	iPTF13asv	super-Chandrasekhar
B-band peak magnitude	$-18 \sim -19.5$	-19.97 ± 0.06	< -19.6
UV peak magnitude	$\gtrsim -15$	-15.25	$\lesssim -15$
Δm_{15} (mag)	$0.8 \sim 1.2$	1.0	$\simeq 0.6$
Near-IR secondary peak	strong	strong	weak or absent
Carbon feature after max	no	weak	strong
Si II 6355 velocity at max (10^3 km s^{-1})[a]	$10 \sim 14$	10	$8 \sim 12$
Si II 6355 velocity gradient at max (km s^{-1} day^{-1})[a]	$50 - 150$	~ 0	$-72 \sim 46$
^{56}Ni mass ($M_\odot$)[b]	$0.3 \sim 0.6$	$0.81^{+0.10}_{-0.18}$	> 0.75
Ejecta mass ($M_\odot$)[b]	$0.8 \sim 1.5$	$1.44^{+0.44}_{-0.12}$	> 1.5

[a] The velocity measurements of normal events are from Foley et al. (2011). Those of super-Chandrasekhar events are from Scalzo et al. (2012).
[b] The mass measurements of normal events are from Scalzo et al. (2014b). Those of super-Chandrasekhar events are from Scalzo et al. (2012).

As a result of the above analysis, we are forced to conclude that the strong UV emission is intrinsic. In fact, the strong UV emission and the lack of iron in early-phase spectra may be causally related. The latter implies an ejecta structure of weak mixing with most iron group elements concentrated in the low-velocity zones of the ejecta. Since the line blanketing of iron group elements dominates the UV opacity, the optical opacity of UV photons is very small until the photosphere recedes into the low-velocity zones of the ejecta. Consequently, the SN appears to be more UV luminous around maximum. The concentration of iron group elements is also supported by the strong secondary peak in the near-IR. The near-IR secondary peak results from transition of iron group elements from doubly ionized states to singly ionized states. The double-peaked morphology of the near-IR light curve is therefore a direct consequence of the abundance stratification of the ejecta, in particular, the concentration of iron group elements in the central regions (Kasen 2006). To sum up, all these observational facts suggest that iPTF13asv has a stratified ejecta with strong concentration of iron group elements in the center.

5.3. *Progenitor*

The similarity to super-Chandrasekhar events and the derived ejecta mass naturally suggest that the progenitor of iPTF13asv is a DD system. This is further supported by the stratified ejecta. Hydrodynamic simulations (e.g., Kromer et al. 2010; Sim et al. 2013) show that explosions in a SD system cannot avoid a certain level of mixing in the ejecta. Hence, these models have difficulty in concentrating most of iron group elements in the center of the ejecta. For merging WDs, in contrast, simulations of prompt detonation (e.g., Moll et al. 2014) produce strongly stratified structures along polar directions in asymmetric ejecta. In these directions, iron group elements are confined in the low-velocity regions. Hence, based on these arguments, we infer that iPTF13asv originates from a DD system.

5.4. *UV-Luminous Type Ia SNe At High Redshifts*

Spectroscopic classification for high-redshift SNe requires very long integration on big telescopes. Therefore, in high-redshift SN surveys, an optical-UV "dropout" is introduced to preselect Type Ia candidates (for example, Riess et al. 2004, 2007). In practice, the F850LP, F775W and F606 filters on the *HST* Advanced Camera for Survey (ACS) are usually used to search for SNe at redshifts up to 1.8.

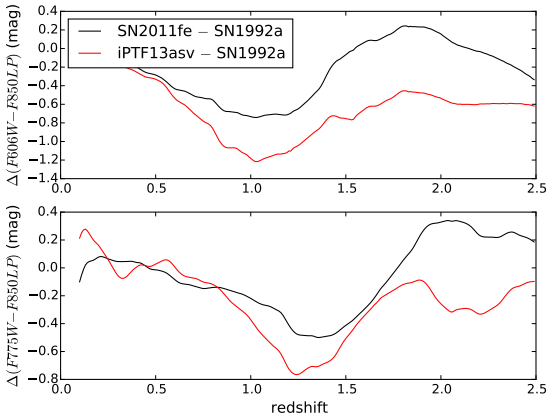

Figure 14. Color difference as a function of redshift for three different SNe Ia.

The color preselection criteria may introduce bias by ignoring UV-luminous SNe. In Figure 14, we calculate the color difference in the F850LP, F775W and F606 filters for normal SN1992a (Kirshner et al. 1993), near-UV blue SN2011fe (Mazzali et al. 2014) and UV-luminous iPTF13asv at different redshifts. As can be seen, the three SNe show different colors at high redshifts. Although the rate of iPTF13asv-like events is probably low in the nearby Universe, there might be more such SNe at high redshifts, as there are more metal-poor dwarf galaxies at high redshifts. Hence it might become an unnegligible component in estimating the SN rate at high redshifts.

6. CONCLUSION

In this paper, we present multi-wavelength observations of a peculiar over-luminous Type Ia supernova, iPTF13asv, discovered by the intermediate Palomar Transient Factory. While its $\Delta m_{15} = 1.03 \pm 0.01$ mag and sharp secondary near-IR peak resemble characteristic features of normal Type Ia supernovae, iPTF13asv shows low but almost constant expansion velocities and persistent carbon absorption features after the maximum, both of which are commonly seen super-Chandrasekhar

events. We derive a ^{56}Ni mass of $0.81^{+0.10}_{-0.18}M_{\odot}$ and a total ejecta mass of $1.44^{+0.44}_{-0.12}M_{\odot}$. Therefore, we suggest that iPTF13asv is an intermediate case between the normal and super-Chandrasekhar events.

Our observations of iPTF13asv also show an absence of iron absorption features in its early-phase spectra until several days before maximum, and strong UV emission around peak. These observations together with sharp near-IR secondary maxima indicate that iPTF13asv has a stratified structure along the line of sight, with synthesized iron group elements concentrated in the center of its ejecta. Compared to hydrodynamic simulations, only WD mergers might produce the inferred ejecta structure. Therefore, based on the stratified ejecta and its similarity to super-Chandrasekhar events, we conclude that iPTF13asv originates from a double-degenerate progenitor system.

We speculate that iPTF13asv might be a transiting case between normal and super-Chandrasekhar events. Moving forward, the current and upcoming time-domain surveys, such as the Zwicky Transient Facility, will find many more Type Ia supernovae of different subclasses. Equipped with fast-turnaround follow-up observations which allow us to estimate the ejecta mass and the ^{56}Ni mass, these surveys will map how observational features vary as a function the total ejecta mass for supernovae from the double-degenerate channel. In particular, UV photometry and optical spectroscopy of these supernovae at early phases will encode information about mixing of iron group elements.

We thank M. Kromer for useful discussion. We are also grateful to A. De Cia, O. Yaron, D. Tal, D. Perley, K. Tinyanont, A. Waszczak, I. Arcavi, and S. Tang for doing observation and data reduction. This research is partly supported by the *Swift* Guest Investigator program and by the National Science Foundation through the Global Relay of Observatories Watching Transients Happen program. A.G. and R.A. acknowledge support from the Swedish Research Council and the Swedish Space Board. E. Y. H. acknowledges the support provided by the Danish Agency for Science and Technology and Innovation through a Sapere Aude Level 2 grant.

The data presented here were obtained in part with ALFOSC, which is provided by the Instituto de Astrofisica de Andalucia (IAA) under a joint agreement with the University of Copenhagen and NOTSA. We thank the RATIR project team and the staff of the Observatorio Astronómico Nacional on Sierra San Pedro Mártir. RATIR is a collaboration between the University of California, the Universidad Nacional Autónoma de México, NASA Goddard Space Flight Center, and Arizona State University, benefiting from the loan of an H2RG detector and hardware and software support from Teledyne Scientific and Imaging. RATIR, the automation of the Harold L. Johnson Telescope of the Observatorio Astronómico Nacional on Sierra San Pedro Mártir, and the operation of both are funded through NASA grants NNX09AH71G, NNX09AT02G, NNX10AI27G, and NNX12AE66G, CONACyT grants LN 260369, and UNAM PAPIIT grant IG100414.

A portion of this work was carried out at the Jet Propulsion Laboratory, under contract with the National Aeronautics and Space Administration.

REFERENCES

Aldering, G., Antilogus, P., Bailey, S., et al. 2006, ApJ, 650, 510
Barone-Nugent, R. L., Lidman, C., Wyithe, J. S. B., et al. 2012, MNRAS, 425, 1007
Betoule, M., Kessler, R., Guy, J., et al. 2014, A&A, 568, A22
Breeveld, A. A., Landsman, W., Holland, S. T., et al. 2011, in American Institute of Physics Conference Series, Vol. 1358, American Institute of Physics Conference Series, ed. J. E. McEnery, J. L. Racusin, & N. Gehrels, 373–376
Brown, P. J. 2014, ApJ, 796, L18
Brown, P. J., Dawson, K. S., de Pasquale, M., et al. 2012, ApJ, 753, 22
Brown, P. J., Kuin, P., Scalzo, R., et al. 2014, ApJ, 787, 29
Burns, C. R., Stritzinger, M., Phillips, M. M., et al. 2014, ApJ, 789, 32
Cao, Y., Kulkarni, S. R., Howell, D. A., et al. 2015, Nature, 521, 328
Cenko, S. B., Fox, D. B., Moon, D.-S., et al. 2006, PASP, 118, 1396
Fitzpatrick, E. L. 1999, PASP, 111, 63
Foley, R. J., McCully, C., Jha, S. W., et al. 2014, ApJ, 792, 29
Foley, R. J., Sanders, N. E., & Kirshner, R. P. 2011, ApJ, 742, 89
Foster, C., Hopkins, A. M., Gunawardhana, M., et al. 2012, A&A, 547, A79
Goobar, A., & Leibundgut, B. 2011, Annual Review of Nuclear and Particle Science, 61, 251
Goobar, A., Kromer, M., Siverd, R., et al. 2015, ApJ, 799, 106
Guy, J., Astier, P., Baumont, S., et al. 2007, A&A, 466, 11
Hicken, M., Garnavich, P. M., Prieto, J. L., et al. 2007, ApJ, 669, L17
Hoeflich, P., & Khokhlov, A. 1996, ApJ, 457, 500
Howell, D. A., Sullivan, M., Nugent, P. E., et al. 2006, Nature, 443, 308
Hsiao, E. Y., Conley, A., Howell, D. A., et al. 2007, ApJ, 663, 1187
Hsiao, E. Y., Marion, G. H., Phillips, M. M., et al. 2013, ApJ, 766, 72
Jeffery, D. J. 1999, ArXiv Astrophysics e-prints, astro-ph/9907015
Jeffery, D. J., Branch, D., & Baron, E. 2006, ArXiv Astrophysics e-prints, astro-ph/0609804
Kasen, D. 2006, ApJ, 649, 939
—. 2010, ApJ, 708, 1025
Kelly, P. L., Fox, O. D., Filippenko, A. V., et al. 2014, ApJ, 790, 3
Kennicutt, Jr., R. C. 1998, ARA&A, 36, 189
Kirshner, R. P., Jeffery, D. J., Leibundgut, B., et al. 1993, ApJ, 415, 589
Kriek, M., van Dokkum, P. G., Labbé, I., et al. 2009, ApJ, 700, 221
Kromer, M., Sim, S. A., Fink, M., et al. 2010, ApJ, 719, 1067
Kushnir, D., Katz, B., Dong, S., Livne, E., & Fernández, R. 2013, ApJ, 778, L37
Lantz, B., Aldering, G., Antilogus, P., et al. 2004, in Society of Photo-Optical Instrumentation Engineers (SPIE) Conference Series, Vol. 5249, Optical Design and Engineering, ed. L. Mazuray, P. J. Rogers, & R. Wartmann, 146–155
Law, N. M., Kulkarni, S. R., Dekany, R. G., et al. 2009, PASP, 121, 1395
Li, W., Bloom, J. S., Podsiadlowski, P., et al. 2011, Nature, 480, 348
Lundqvist, P., Nyholm, A., Taddia, F., et al. 2015, A&A, 577, A39
Maeda, K., & Iwamoto, K. 2009, MNRAS, 394, 239
Maoz, D., Mannucci, F., & Nelemans, G. 2014, ARA&A, 52, 107
Margutti, R., Parrent, J., Kamble, A., et al. 2014, ApJ, 790, 52
Marion, G. H., Brown, P. J., Vinkó, J., et al. 2015, ArXiv e-prints, arXiv:1507.07261
Mazzali, P. A., Sullivan, M., Hachinger, S., et al. 2014, MNRAS, 439, 1959
McCully, C., Jha, S. W., Foley, R. J., et al. 2014, Nature, 512, 54
Milne, P. A., Brown, P. J., Roming, P. W. A., Bufano, F., & Gehrels, N. 2013, ApJ, 779, 23
Moll, R., Raskin, C., Kasen, D., & Woosley, S. E. 2014, ApJ, 785, 105
Nadyozhin, D. K. 1994, ApJS, 92, 527
Nobili, S., & Goobar, A. 2008, A&A, 487, 19
Nomoto, K., & Iben, Jr., I. 1985, ApJ, 297, 531
Nugent, P., Kim, A., & Perlmutter, S. 2002, PASP, 114, 803
Nugent, P. E., Sullivan, M., Cenko, S. B., et al. 2011, Nature, 480, 344
Oke, J. B., & Gunn, J. E. 1982, PASP, 94, 586

Pan, Y.-C., Sullivan, M., Maguire, K., et al. 2014, MNRAS, 438, 1391
Parrent, J. T., Thomas, R. C., Fesen, R. A., et al. 2011, ApJ, 732, 30
Patat, F., Chandra, P., Chevalier, R., et al. 2007, Science, 317, 924
Phillips, M. M. 1993, ApJ, 413, L105
Piro, A. L. 2012, ApJ, 759, 83
Piro, A. L., & Morozova, V. S. 2015, ArXiv e-prints, arXiv:1512.03442
Planck Collaboration, Ade, P. A. R., Aghanim, N., et al. 2013, ArXiv e-prints, arXiv:1303.5076
Poznanski, D., Prochaska, J. X., & Bloom, J. S. 2012, MNRAS, 426, 1465
Rau, A., Kulkarni, S. R., Law, N. M., et al. 2009, PASP, 121, 1334
Riess, A. G., Strolger, L.-G., Tonry, J., et al. 2004, ApJ, 600, L163
Riess, A. G., Strolger, L.-G., Casertano, S., et al. 2007, ApJ, 659, 98
Scalzo, R., Aldering, G., Antilogus, P., et al. 2012, ApJ, 757, 12
—. 2014a, MNRAS, 440, 1498
Scalzo, R. A., Ruiter, A. J., & Sim, S. A. 2014b, MNRAS, 445, 2535
Scalzo, R. A., Aldering, G., Antilogus, P., et al. 2010, ApJ, 713, 1073
Scalzo, R. A., Childress, M., Tucker, B., et al. 2014c, MNRAS, 445, 30
Schlafly, E. F., & Finkbeiner, D. P. 2011, ApJ, 737, 103
Shappee, B. J., Stanek, K. Z., Pogge, R. W., & Garnavich, P. M. 2013, ApJ, 762, L5
Silverman, J. M., & Filippenko, A. V. 2012, MNRAS, 425, 1917
Silverman, J. M., Ganeshalingam, M., Li, W., et al. 2011, MNRAS, 410, 585
Sim, S. A., Seitenzahl, I. R., Kromer, M., et al. 2013, MNRAS, 436, 333
Stanishev, V., Goobar, A., Amanullah, R., et al. 2015, ArXiv e-prints, arXiv:1505.07707
Sternberg, A., Gal-Yam, A., Simon, J. D., et al. 2014, MNRAS, 443, 1849
Sullivan, M., Guy, J., Conley, A., et al. 2011, ApJ, 737, 102
Swartz, D. A., Sutherland, P. G., & Harkness, R. P. 1995, ApJ, 446, 766
Thomas, R. C., Nugent, P. E., & Meza, J. C. 2011a, PASP, 123, 237
Thomas, R. C., Aldering, G., Antilogus, P., et al. 2011b, ApJ, 743, 27
Vinkó, J., Sárneczky, K., Takáts, K., et al. 2012, A&A, 546, A12
Whelan, J., & Iben, Jr., I. 1973, ApJ, 186, 1007
Yamanaka, M., Kawabata, K. S., Kinugasa, K., et al. 2009, ApJ, 707, L118
Yaron, O., & Gal-Yam, A. 2012, PASP, 124, 668
Yoon, S.-C., & Langer, N. 2005, A&A, 435, 967
Yuan, F., Quimby, R. M., Wheeler, J. C., et al. 2010, ApJ, 715, 1338
Zhou, L., Wang, X., Zhang, K., et al. 2013, Central Bureau Electronic Telegrams, 3543, 1